

---

# LTAU–FF: LOSS TRAJECTORY ANALYSIS FOR UNCERTAINTY IN ATOMISTIC FORCE FIELDS

---

**Joshua A. Vita\***

Lawrence Livermore National Laboratory  
Livermore, California 94550, USA

**Amit Samanta**

Lawrence Livermore National Laboratory  
Livermore, California 94550, USA

**Fei Zhou**

Lawrence Livermore National Laboratory  
Livermore, California 94550, USA

**Vincenzo Lordi**

Lawrence Livermore National Laboratory  
Livermore, California 94550, USA

## ABSTRACT

Model ensembles are simple and effective tools for estimating the prediction uncertainty of deep learning atomistic force fields. Despite this, widespread adoption of ensemble-based uncertainty quantification (UQ) techniques is limited by the high computational costs incurred by ensembles during both training and inference. In this work we leverage the cumulative distribution functions (CDFs) of per-sample errors obtained over the course of training to efficiently represent the model ensemble, and couple them with a distance-based similarity search in the model latent space. Using these tools, we develop a simple UQ metric (which we call LTAU) that leverages the strengths of ensemble-based techniques without requiring the evaluation of multiple models during either training or inference. As an initial test, we apply our method towards estimating the epistemic uncertainty in atomistic force fields (LTAU–FF) and demonstrate that it can be easily calibrated to accurately predict test errors on multiple datasets from the literature. We then illustrate the utility of LTAU–FF in two practical applications: 1) tuning the training–validation gap for an example dataset, and 2) predicting errors in relaxation trajectories on the OC20 IS2RS task. Though in this work we focus on the use of LTAU with deep learning atomistic force fields, we emphasize that it can be readily applied to any regression task, or any ensemble-generation technique, to provide a reliable and easy-to-implement UQ metric.

## 1 Introduction

In computational chemistry and materials science, deep learning force fields have become a standard tool for accelerating quantum mechanical calculations [DCC19, MHW20, Mis21]. The goal of these force fields is to perform a regression task to reproduce the potential energy surface of a system in a computationally efficient way. This is done by learning to predict the energies and atomic forces from a high-accuracy ground truth, such as density functional theory (DFT) calculations or similar methods. A number of different approaches to this problem have been developed over the years, including the use of Gaussian processes [BPKC10, CBFvL20], symbolic regression [HBY<sup>+</sup>19], feed-forward neural networks [BP07, MC20], and message-passing neural networks [BMS<sup>+</sup>22, BKS<sup>+</sup>22], among others. However, with the transition away from more interpretable, classical physics-based force fields [Jon24, Bas92, vDDL01], questions surrounding the necessary complexity of model architectures, and the domains over which they are valid, have become prevalent. Hence, developing UQ methods accounting for different sources of epistemic uncertainty, therefore helping to isolate the effects of model uncertainty, is a primary concern of force field developers.

While multiple UQ techniques have been applied to atomistic force fields, including dropout neural networks [WT20], Bayesian frameworks [APK12, XVS<sup>+</sup>21], or Gaussian mixture models [ZBMK23], by far the most popular approach in practice is the use of ensemble-based methods, where the ensemble variance is taken as a measure of the pre-

---

\*Correspondence to: [vita1@llnl.gov](mailto:vita1@llnl.gov)

dictive uncertainty of the model. Particularly beneficial is the fact that these ensemble methods do not require any modifications to the model architecture or training algorithm, and can therefore be readily applied to any existing development workflow. Due in large part to this simplicity and generalizability, ensemble-based UQ techniques have been widely applied towards numerous machine learning and deep learning tasks [LPB16, ZLP<sup>+</sup>22], and are often considered to be the gold standard when evaluating the performance of new UQ methods for atomistic force fields [BBJB<sup>+</sup>21, HSY<sup>+</sup>20, WSC21, CMCW<sup>+</sup>23, ZBMK23, WGC<sup>+</sup>23].

Despite their ubiquity, ensemble methods typically suffer from two main drawbacks: high computational costs (for both training and inference) and difficulties maintaining ensemble diversity resulting in poor uncertainty estimates. In particular, ensemble sizes of approximately 5 to 30 models have been found to be necessary for various practical applications of UQ for force fields [GBM17, LGC<sup>+</sup>23], making ensemble-based methods potentially infeasible for large training sets or expensive models. Furthermore, although ensemble-based UQ techniques have still been shown to out-perform single-model methods [TUG<sup>+</sup>23], there is growing evidence that they result in overconfident UQ measures [KZ22, LGC<sup>+</sup>23]. Similar issues have been documented in other deep learning applications, where the overconfidence is attributed to a lack of ensemble diversity [FHL19, EMR<sup>+</sup>22, ZLP<sup>+</sup>22], which in turn stems from the methods used to generate the ensemble. Intuitively, the most straightforward approaches to ensemble generation (training multiple models with different initial weights, data splits, or training hyperparameters [PCK17]) will only sample models at different local minima of the loss function, and therefore fail to account for the full topography of the loss surface, which has been shown in many cases to correlate with generalization error [HS94, CCS<sup>+</sup>16, LXT<sup>+</sup>17, GGG<sup>+</sup>21, VSK23].

In this work, we develop the new LTAU method, which is an ensemble-based technique that addresses the issues of computational cost and ensemble diversity, and can be broadly applied to any force field or other regression task. Specifically, we provide the following contributions:

- We outline our proposed method, LTAU, which utilizes the cumulative distribution function (CDF) of errors sampled during training to provide estimates of the likelihood that a model’s predictions will fall below a chosen tolerance threshold. This use of the training error trajectories imposes no additional computational overhead and inherently improves the diversity of the ensemble by incorporating additional information from various points on the loss landscape.
- By coupling the CDF to a nearest-neighbor search in the model’s latent space, we show how LTAU can provide a cheap, easy-to-implement UQ measure that does not require evaluating an ensemble during inference, thus eliminating a major barrier to the application of ensemble-based UQ techniques with large models.
- We apply our method towards UQ in atomistic force fields (LTAU-FF) and show that it accurately estimates in-domain (ID) errors and can be readily tuned to improve calibration on out-of-domain (OOD) predictions for a variety of benchmarking datasets.
- Finally, to demonstrate the utility of LTAU-FF in practical applications, we conduct two experiments: 1) re-weighting the training set of the model to prioritize high or low confidence samples, and 2) applying our method to the IS2RS task from the OC20 challenge to predict errors in relaxation trajectories. From these experiments, we observe that the UQ metric can be used to tune the training-validation performance gap and can also serve as a reliable indicator of model performance in real-world applications and on large-scale datasets.

## 2 Background

The defining trait of the LTAU method developed in this work, which distinguishes it from other ensemble-based UQ methods, is its ability to leverage information from large ensembles of models while only having to evaluate a single model during inference. This is achieved through efficient use of logged error trajectories sampled during training and a similarity search in the model’s latent space during inference. The method builds heavily upon two key concepts in deep learning: training trajectory analysis and distance-based UQ.

### 2.1 Training trajectory analysis

Training trajectories have been used in a number of deep learning applications for the purpose of outlier detection [SSL<sup>+</sup>20, PZEW20, ADH20, PGD21, SCQvdS23], data pruning [TSC<sup>+</sup>18, MBL19, KSRI20, KSR<sup>+</sup>21, SGS<sup>+</sup>22, SCQvdS23], and influence estimation [Fel19, FZ20, GWP<sup>+</sup>23]. These approaches have leveraged the rich information that is sampled over the course of training, including loss gradients [PLSK20, KSRI20, KSR<sup>+</sup>21, MBL19, PGD21, MBL19, ADH20], Softmax outputs [SSL<sup>+</sup>20, RTH<sup>+</sup>22], or other custom metrics [PZEW20, TSC<sup>+</sup>18, FZ20,

SCQvdS23]. However, many of these metrics have been designed primarily for classification tasks (i.e., they are derived using assumptions about the loss function or model architecture that are unique to classification) and require modification in order to be applied in regression settings.

Most relevant to this work is the concept of **confidence** [SSL<sup>+</sup>20], which utilizes the Softmax outputs obtained during training to characterize the model’s confidence in a given prediction. Specifically, the model is said to be “confident” in its prediction for a given point if the point has a high probability of being correctly predicted (i.e., high average Softmax activation) throughout the course of training. We chose to build on this notion of confidence for two reasons: first, it is intuitive to understand in the context of UQ (i.e., high confidence implies low uncertainty, and low confidence implies high uncertainty); and second, it can be efficiently computed in post-processing. As will be discussed in Section 3.4, in this work we use the evaluation of a sample’s CDF of errors at a chosen tolerance threshold as the measure of the model’s confidence on that sample.

## 2.2 Distance-based UQ

A critical assumption of the method developed in this work is that points which are close to each other in the model’s latent space also have similar CDFs, which is a concept that is discussed further in Appendix D. On a smoothly-varying manifold, proximity among points in the latent or input space is often used to infer or model function values. This notion has been successfully applied to develop tools like radial basis functions, Gaussian process regression, and many others. Similarly, this concept has been applied to UQ, where a simple method for estimating the uncertainty in a model’s prediction for a test point is to use the weighted Euclidean distance (in either the input space or a latent space) between the test point and the nearest training point [LW18, APH<sup>+</sup>21, SGS<sup>+</sup>22]. The rationale behind distance-based UQ metrics is that a model is less likely to have accurate predictions on points which are further from the training set. While related methods have been used for UQ with atomistic force fields [JDY<sup>+</sup>19, Per22, ZBMK23], a distance metric alone is insufficient for constructing a well-calibrated UQ metric, and usually requires additional calibration techniques or making assumptions regarding the distribution of errors [HMUM22]. In our analysis, we observe that LTAU-FF can be calibrated using a simple scaling factor, which will be discussed further in Section 4.1.

## 3 Methods

### 3.1 Model

We use the NequIP model [BMS<sup>+</sup>22] as the deep learning force field in this work. NequIP is a graph-based message-passing neural network that uses spherical harmonics to represent local atomic environments with equivariance. The use of message-passing and equivariant features, respectively, have been shown to be useful for incorporating long-range interactions in the model and avoiding issues caused by the inability of invariant models to distinguish between symmetrically-equivalent atomic environments [BBK<sup>+</sup>22]. NequIP has achieved state-of-the-art performance for a number of applications [SUG21, RNE<sup>+</sup>22]. The hyperparameters of the model are adjusted for each dataset, with details provided in Appendix A.

### 3.2 Datasets

Three training datasets are used in this work: 3BPA [KOK<sup>+</sup>21], Carbon\_GAP\_20 [RDG<sup>+</sup>20], and the 200k split of the S2EF task from the OC20 challenge [CDG<sup>+</sup>21b]. These datasets were chosen deliberately to provide systematic tests of the limitations of our method with increasingly complex data. We start with a simple molecular test case for refining our methods (3BPA), then expand to a more diverse dataset typical of solid-state force field fitting tasks (Carbon\_GAP\_20), and finally test against a challenging real-world application (IS2RS task from OC20). Detailed descriptions of the datasets are found in Appendix B and the referenced citations. All datasets are available from their original sources.

### 3.3 Training details

For the most part, standard published hyperparameters were used for training, with details provided in Appendix A. As a notable exception, for the 3BPA and Carbon\_GAP\_20 datasets, we trained models **only to forces**, which is in contrast to typical force field fitting workflows that usually also include an energy term in the loss function. We chose to weight the energy contributions to 0.0 in these cases to remove any possible spurious correlations caused by coupling between the energy and force terms in the loss function, which may have interfered with the UQ analysis. For the OC20 dataset, we weighted the energy term to 1.0 to help avoid unexpected behavior during energy minimization; we note that this

still resulted in strong correlation between the UQ metric provided by LTAU-FF and the accuracy of the predicted ground-state structure, as shown in Section 4.3.

### 3.4 LTAU-FF

As the primary contribution of this paper, we propose the **Loss Trajectory Analysis for Uncertainty (LTAU)** method (Algorithm 1 and Algorithm 2), and demonstrate its application to atomistic force fields (LTAU-FF: LTAU for atomistic Force Fields). The LTAU method builds upon the concepts described in Section 1, using the errors of the ensemble of models sampled during training to approximate the CDF, then coupling the approximated CDF to a distance-based similarity search for estimating uncertainty on test predictions. Implementing LTAU in an existing workflow will typically only require patching existing training code to log per-sample errors at every epoch and adding some basic post-processing. We provide post-processing code and other utility functions for working with the specific models presented in this work (see Section 6).

Central to the LTAU technique is the notion of sample confidence, as described in Section 2.1. In [SSL<sup>+</sup>20], sample confidence is defined as the mean probability of the correct class label being predicted across training epochs and is computed using the outputs of the final Softmax layer. Since regression tasks do not normally use a Softmax output layer and there is no binary notion of “correctness,” we instead choose to use the CDF of errors evaluated at a chosen tolerance threshold,  $atol$ , as the measure of confidence. In this sense, a sample with high confidence is one which has a high probability of having errors below the tolerance threshold over the course of training.

---

**Algorithm 1:** Compute per-sample uncertainties for training points

---

**Input** : An untrained model,  $\mathcal{F}$ ; a training set  $\mathcal{S}$  of size  $N$ ; the number of training epochs,  $E$

**Output:** The uncertainty of each training point,  $p = \{p_1, \dots, p_N\}$

---

```

1 for  $e = 1 \dots E$  do
2   | Train( $\mathcal{F}$ )
3   | Log(Error( $\mathcal{F}, \mathcal{S}$ ),  $e$ )
4 end
5  $atol = MAE(\mathcal{F}, \mathcal{S})$ 
  // load ExN matrix of trajectories
6  $T \leftarrow LoadErrorTrajectories()$ 
  // return 1xN probabilities array
7  $p = T \leq atol$ 
8 return  $1 - \frac{1}{E} \sum_e p^e$ 
```

---

For LTAU-FF, the first step to computing the sample confidence in this manner is to train a model and log the errors at every epoch (Algorithm 1). By logging the model’s errors on every sample (i.e., every atom) at every epoch, we can construct error trajectories  $T_i = \{\epsilon_i^1, \dots, \epsilon_i^E\}$  for every atom  $i$ , where  $\epsilon_i^t = |F_{i,DFT} - \hat{F}_i^t|_2$  is the  $L_2$  norm of the force error vector for atom  $i$  at the end of epoch  $t$ , and  $E$  is the total number of training epochs. We will then define the model’s confidence in its prediction of the forces for atom  $i$  as  $p_i = P(\epsilon_i^t \in T_i \leq atol)$ , where  $atol$  is a chosen absolute error tolerance threshold. This corresponds to the CDF of the errors evaluated at  $atol$ , and can be easily computed in post-processing after logging the per-sample errors at each epoch. A reasonable choice for  $atol$  would be the mean absolute error (MAE) of the optimal model, since  $p_i$  could then be interpreted as the confidence that the model’s predictions on atom  $i$  will be below the MAE. Alternatively, one could tune  $atol$  in order to maximize the “dispersion” [TNY<sup>+</sup>20] of the UQ metric. This method can be easily extended to incorporate relative errors by defining  $p_i = P(\epsilon_i^t \in T_i \leq atol + rtol \times |F_{i,DFT}|_2)$ , where  $rtol$  is a relative error threshold; however, for the sake of simplicity we will only use  $rtol = 0$ . We note that instead of using the  $L_2$  norm for computing  $\epsilon_i$ , each Cartesian coordinate could be treated individually, yielding  $\epsilon_{ic}$  (with  $c$  indexing the Cartesian direction). This would allow uncertainties to be obtained along each axis, but would incur higher memory costs when logging the per-sample errors. Finally, alternative error metrics can also be used instead of the MAE – for example, the mass-normalized errors explored in [WWS<sup>+</sup>23] would be particularly useful for multi-element systems.

In order to use the  $p_i$  values computed on the training set for predicting uncertainties on a test point,  $j$ , we compute  $p_j = \frac{1}{k} \sum_{i \in \mathcal{N}_j} p_i$ , the average of the  $p_i$  values for the nearest  $k$  samples,  $\mathcal{N}_j$ , from the training set (Algorithm 2). The  $k$  nearest neighbors are obtained by performing a similarity search in the latent space of the model; specifically, using the output of the last message-passing layer of the NequIP model (prior to the linear readout layers) as the atomic descriptor. This means that we must evaluate the model for the full training set, store the latent descriptors for all training atoms, then compare the descriptors for each test atom,  $j$ . The cost of computing  $p_j$  then necessarily scales



---

**Algorithm 2:** Compute uncertainty on a test point

---

**Input** : A trained model,  $\mathcal{F}$ ; a training set  $\mathcal{S}$ ; the training uncertainties,  $p$ ; a test point,  $x_j$ ; the number of nearest neighbors to search for,  $k$

**Output:** The uncertainty of the prediction on the test point,  $p_j$

- 1  $D \leftarrow \text{Descriptors}(\mathcal{F}, \mathcal{S})$
  - 2  $d_j \leftarrow \text{Descriptor}(\mathcal{F}, x_j)$
  - 3  $\mathcal{N}_j \leftarrow \text{NearestNeighbors}(d_j, D, k)$
  - 4 return  $\frac{1}{k} \sum_{i \in \mathcal{N}_j} p_i$
- 

with the size of the training set. Since typical training sets for force fields can include  $\mathcal{O}(10^4)$  -  $\mathcal{O}(10^7)$  atoms, we rely upon the FAISS [JDJ19] package for efficiently searching for the  $k$  nearest neighbors of test points. Additional details regarding the FAISS hyperparameters used in this work can be found in Appendix A.

In developing the LTAU method, we found that computing  $p_i$  using an ensemble of  $M$  models was often valuable in order to obtain better-converged values, especially when working with datasets for which noisier  $p_i$  values were observed. Although the  $p_i$  values can already be thought of as being computed over an ensemble of models (sampled during training), additionally averaging them over a second ensemble (sampled from different training runs) helps to more thoroughly sample the loss landscape of the model, thus resulting in a metric which can be expected to better reflect the true behavior of the model [FHL19]. In this work, we used ensembles of  $M = 1, 10$ , or  $20$  models for computing  $p_i$  values for the OC20, 3BPA, or Carbon\_GAP\_20 datasets, respectively, which we observed resulted in reasonable convergence of the metric (see Fig. C3). Throughout the remainder of this paper, we will explicitly use the notation  $\mu_M(\cdot)$  or  $\sigma_M(\cdot)$  any time a value is being computed as an ensemble average (or standard deviation). We emphasize that while the use of an ensemble increases the training cost, it does *not* affect the cost of inference since LTAU only relies upon the  $\mu_M(p_i)$  values (which are computed once during post-processing, then cached) and the latent descriptors extracted from the single model being used for inference. Furthermore, the use of  $M = 1$  for the OC20 dataset shows that the method is still viable even in scenarios where it is impractical or not possible to train multiple models. Additional analysis of the effects of  $M$  and training duration on  $\mu_M(p_i)$  and  $\sigma_M(p_i)$  can be found in Appendix C.

The LTAU method outlined above is closely related to the notion of “checkpoint ensembles” [CLL17], which have been used previously as an efficient alternative to traditional ensemble sampling techniques. We note, however, that checkpoint ensembles still require evaluating all models in the ensemble during inference, and therefore suffer from the same limitations as traditional ensemble UQ methods due to their computational costs. In contrast, LTAU uses a neighbor lookup along with the pre-computed  $p_i$  values, which is significantly less expensive than even a single model forward pass (see Section 4.4 for details on computational cost). Furthermore, it is worth highlighting that although in this work we use the ensemble of models obtained during training, LTAU can be coupled with any existing ensemble-generation technique by instead computing the per-sample error CDFs over the desired ensemble. This flexibility means that the ensemble used for LTAU can be adjusted to better capture the desired source of uncertainty (e.g., parametric vs. model uncertainty).

## 4 Results and Discussion

### 4.1 Calibrating LTAU-FF

As an initial test of the accuracy of LTAU-FF in estimating errors on force predictions, we train ensembles of models to the 3BPA and Carbon\_GAP\_20 datasets, then qualitatively compare the calibration curves of the model on subsets of the test data, as is done in [TNY+20]. We generate calibration curves shown in Fig. 1 and Fig. 2 by first binning test points based on their  $p_j$  values, then plotting the observed percentage of points in each bin with errors below the threshold. Since the  $p_j$  values are directly interpretable as the predicted likelihood of falling below the threshold, we can easily see if they are well-calibrated based on how close the resultant curves are to the ideal  $x = y$  line (shown with the red dashed line). In general, we observed that the calibration to in-domain data can be improved by tuning the number of neighbors,  $k$ , over which  $p_j$  values were computed, while calibration to out-of-domain data required re-scaling of the CDF obtained from the training set in order to better match the higher errors observed on the out-of-domain data.

As discussed in [TNY+20], good calibration alone is not a sufficient condition for a suitable UQ metric, since a metric could be well-calibrated while having extremely large uncertainty measures. It is also desirable that a UQ metric be “sharp,” meaning that the uncertainty measures be small in order to provide tighter confidence intervals over the model predictions. In the case of LTAU, the sharpness of the metric can be meaningfully adjusted by tuning the

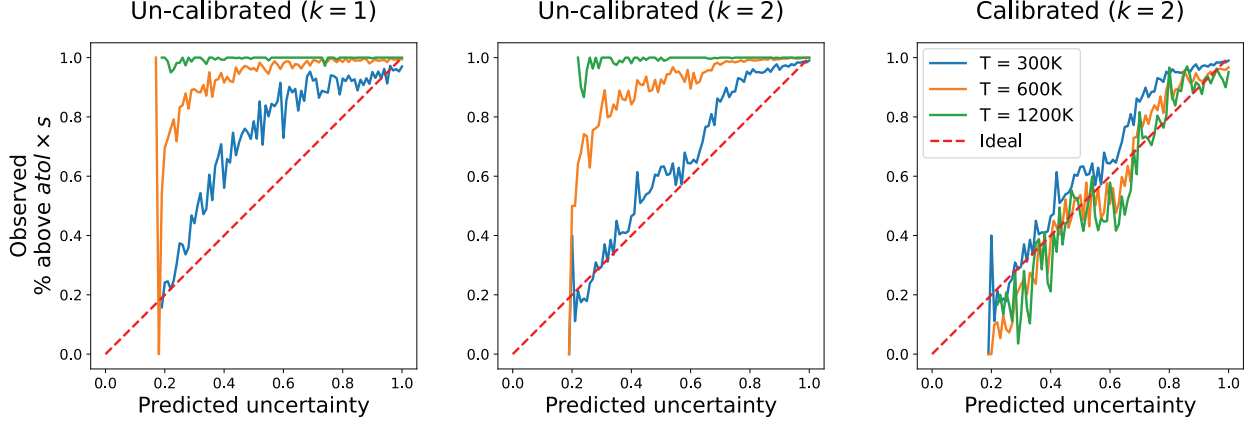


Figure 1: Calibration curves for the 3BPA test sets. Test sets for each temperature are plotted as different colors. Panel **a** averages  $p_i$  values over  $k = 1$  neighbors, while panels **b** and **c** use values of  $k = 2$ . An  $atol$  value of  $0.0075 \text{ eV/\AA}$  was used for all curves in this figure. For the un-calibrated curves (panels **a** and **b**), the scaling factor,  $s$ , is set to 1 for all temperatures. For the calibrated curves (panel **c**),  $s$  has been manually adjusted to 2 and 4 for the 600K and 1200K test sets, respectively.

threshold value  $atol$ . Fig. C1 shows the distributions of  $p_i$  for all datasets explored in this work to guide understandings of how changing  $atol$  can be used to adjust the sharpness of the metric.

### 3BPA

In Fig. 1, we observe that the simplest approach ( $k = 1$ , with no additional calibration) yields reasonable results only for the 300K 3BPA test set. This is not surprising given that the training set was also sampled at 300K, and therefore the 300K test set is likely still predominantly in-domain. Increasing  $k$  to 2 in Fig. 1b, in order to help account for any noise in the  $\mu_M(p_i)$  values within the local neighborhood in the latent space, greatly improves the calibration to the 300K test data. However, in Fig. 1a and Fig. 1b, the  $p_j$  values under-predict the likelihood that the test points will have errors below  $atol$  for the 600K/1200K test sets. We attribute this mis-calibration to the fact that the MAEs for the 600K/1200K test sets are higher than those on the 300K train/test sets ( $0.025$  and  $0.064 \text{ eV/\AA}$  for the 600K/1200K test sets, respectively, as opposed to  $0.011 \text{ eV/\AA}$  for the 300K test set). In order to account for the larger average errors on the higher temperature test sets, in Fig. 1c we introduce a scaling factor,  $s$ , and instead calculate the probability within each bin that the errors fall below  $atol \times s$ . The use of a scaling factor equates to the assumption that the high-temperature CDFs have the same distributions as the low-temperature CDF, but over a wider range of errors, as is discussed further in Appendix D. We observe in Fig. 1c that the scaling factor drastically improves the calibration of the UQ metric, bringing it in line with the performance on the 300K set.

### Carbon\_GAP\_20

The application of LTAU-FF to the Carbon\_GAP\_20 dataset, shown in Fig. 2, helps to highlight some of the challenges associated with calibrating the UQ metric to dissimilar subsets of the dataset. In Fig. 2a it can be seen that although the metric is well-calibrated to the total test set (shown in black), the calibration on individual groups is less accurate. Similar to the results shown for the 3BPA dataset, calibration is improved by increasing  $k$  (note that a higher value of 10 is used here), and a scaling factor is helpful for some of the groups (Amorphous\_Bulk and Amorphous\_Surfaces). However, there are still some notable subsets for which the UQ metric still underestimates (Liquid) or overestimates (Graphene) the observed error distributions regardless of the scaling factor, which is discussed further in Appendix D.

## 4.2 Tuning the training-validation gap

One of the primary uses of sample difficulty metrics in the literature is for dataset construction and pruning [TSC<sup>+</sup>18, SSL<sup>+</sup>20, PGD21], where difficult samples are hypothesized to be essential for fitting to datasets with long-tailed distributions [Fel19, FZ20]. In [SGS<sup>+</sup>22], the role of “easy” and “hard” samples was explored further, demonstrating that in many image classification tasks it was possible to prune significant portions of the training set without hurting test accuracy by only removing the samples which were characterized as being easy according to various metrics. The

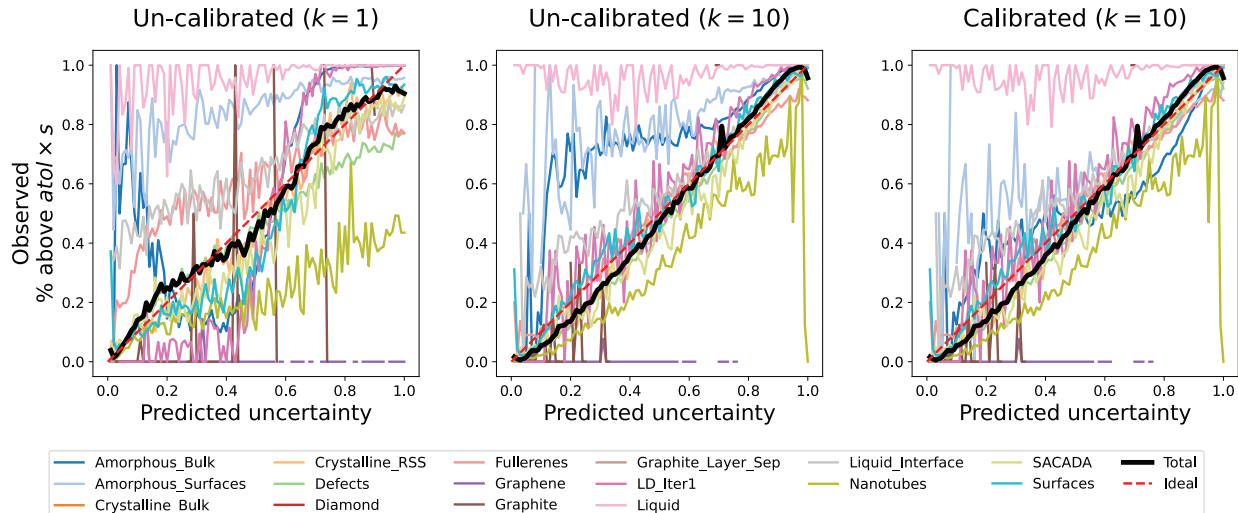


Figure 2: Calibration curves for the Carbon\_GAP\_20 test set. Each `config_type` group is plotted as a different color, and the total test set is plotted in black. Panel **a** uses a value of  $k = 1$ , while panels **b** and **c** use values of  $k = 10$ . An  $atol$  value of  $0.265 \text{ eV/\AA}$  was used for all curves in this figure. For the un-calibrated curves (panels **a** and **b**), the scaling factor,  $s$ , is set to 1 for all groups. For the calibrated curve (panel **c**),  $s$ , has been manually adjusted to 1.3 for the Amorphous\_Bulk and Amorphous\_Surfaces groups. We note that the Liquid and Graphene groups were left un-calibrated because we were unable to identify a suitable  $s$  value.

rationalization given in [SGS<sup>+</sup>22] for this behavior was that easy samples provide coarse-grained information about the target function, while hard samples provide fine-grained information.

If these explanations hold, then it is reasonable to expect that samples from this work with high  $\mu_M(p_i)$  values (i.e., low difficulty) may be useful for constructing more generalizable models, while samples with low  $\mu_M(p_i)$  values (high difficulty) will be useful for improving the quality of fit to data sampled from distributions that are similar to the training set. In order to test if the  $\mu_M(p_i)$  values computed in this work could be used to tune the generalizability of a model, we first trained an ensemble of  $M = 20$  models with uniform weights (in the loss function) for all atoms in the Carbon\_GAP\_20 training set, then used the observed  $\mu_M(p_i)$  values to re-weight the training set and train a new ensemble from scratch. Following the approach taken in [SSL<sup>+</sup>20], we considered both the sample confidence  $\mu_M(p_i)$ , as well as the “variability”,  $\sigma_M(p_i)$ , when re-weighting the training points. Additional details regarding the re-weighting schemes are provided in Appendix E.

As can be seen in Fig. 3, increasing the weights of hard samples (“up-weight hard”) resulted in clear signs of overfitting, where the training MAE was lower than the “uniform” weighting case, but at the expense of higher validation errors. In contrast, increasing the weights of easy samples (“up-weight easy”) helped to reduce the training-validation gap, possibly indicating improved generalizability of the model. While the training-validation gap may have increased further for the up-weight easy scheme with additional training, up-weighting easy samples appears to be a reasonable approach to minimizing the performance gap within a fixed computational budget, although further analysis of this effect is warranted. We further confirmed the performance gaps by computing the ensemble test errors for each weighting scheme, as shown in Fig. E2. Though the test errors followed a similar trend to that seen for the validation errors from Fig. 3, there was a small number of anomalously high errors originating predominantly from the Liquid subset of the test data, which we believe should be investigated manually to confirm convergence and correctness of the DFT-predicted target values.

### 4.3 Leveraging the UQ metric during simulations

The final test of LTAU-FF that we performed was to train a model to the 200k split of the OC20 S2EF task, then to see if LTAU-FF could predict model performance on the IS2RS task. In the IS2RS task, a model is given an initial atomic configuration and is asked to predict the relaxed state, which is a broadly-applicable and extremely valuable task for materials discovery. While some models use the “direct” approach of predicting the relaxed structure directly from the input configuration, an alternative approach (shown to achieve better performance in [CDG<sup>+</sup>21a]) is to perform relaxation via energy minimization, which is what we did in this work.

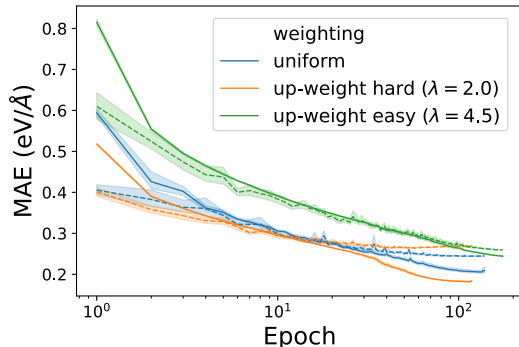


Figure 3: Training (solid lines) and validation (dashed lines) curves for ensembles of  $M = 20$  models trained to the Carbon\_GAP\_20 dataset with different weighting schemes. A random 90:10 training:validation split was used, where all runs used the exact same split. Shaded bands denote the 95% confidence intervals computed across the  $M = 20$  runs for each weighting scheme. Increasing the weight on samples (as described in Appendix E) with low  $\mu_M(p_i)$  values (“up-weight hard”) increased the degree of overfitting, while increasing the weight on samples with high  $\mu_M(p_i)$  (“up-weight easy”) decreased overfitting. The “up-weight easy” models were trained for about 25% longer to improve convergence of the training–validation gap; even longer runs may have widened the gap further, but would have required an unreasonably high computational budget.

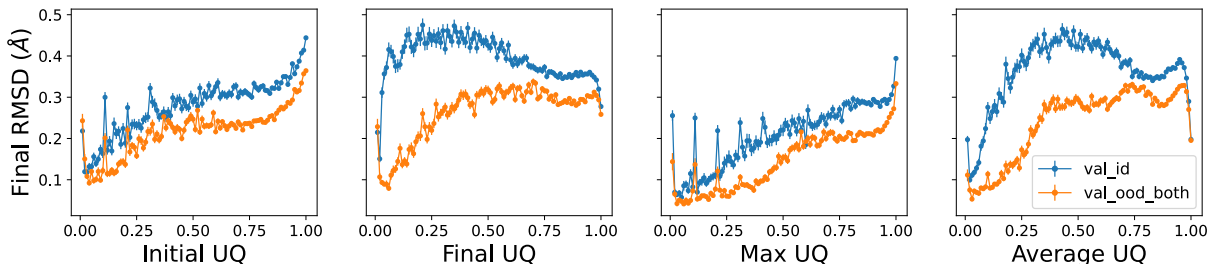


Figure 4: RMSDs between atoms of DFT-relaxed and model-relaxed samples, binned by predicted uncertainty, for OC20. Panels correspond to different choices of snapshot(s) along the relaxation trajectory to use for predicting the final RMSD. The splits identified by [CDG+21b] as being in-domain (val\_id) or out-of-domain (val\_ood\_both) are shown in blue or orange, respectively. Only the “surface” and “adsorbate” atoms are considered in this figure, since the “bulk” atoms are held fixed during energy minimization following the practices outlined in the OC20 IS2RS task. Distances are taken as the average within each bin, and error bars correspond to the standard error for each bin. Note that [CDG+21b] uses a maximum RMSD value of 0.5 Å when computing the “Average Distance within Threshold” (ADwT) metric on the IS2RS task.

A particularly challenging aspect of predicting errors from a relaxation trajectory is that relatively small errors at any point in the trajectory may drastically alter the predicted relaxed structure by causing the model to relax towards an incorrect local energy minimum. Because of this difficulty, in Fig. 4 we consider four possible UQ metrics for predicting the root-mean-square deviation (RMSD) between the true and predicted relaxed structures: the initial, final, maximum, and average UQ value. We observe from Fig. 4 that the initial and maximum uncertainty computed over the full trajectory both show strong correlation with the final RMSD, which matches our expectations that errors in a single step of the trajectory may disrupt the final result. On the other hand, neither the final nor the average UQ value appear to be a good indicator of the final RMSD in this case. Further work is needed to understand how per-atom UQ metrics can be propagated through a trajectory in order to provide uncertainty predictions on dynamical properties.

#### 4.4 Computational cost

To better understand the computational cost of LTAU-FF relative to other aspects of model evaluation, we ran profiling tests computing the atomic forces and uncertainties for 5000 randomly sampled atomic configurations from each test set (500 for 3BPA). These results were obtained using the CPU implementation of FAISS and a TorchScript-compiled NequIP model running on a single NVIDIA V100 GPU. The cost breakdown shown in Table A2 reveals

that computing the  $p_j$  values occupied less than 5% of the walltime, compared to 20-50% for graph construction and 40-70% for the model forward pass.

## 5 Conclusion

In this work, we developed LTAU, a novel UQ method based on the per-sample CDFs obtained during training and a distance-based similarity search, and demonstrated its utility in the field of atomistic simulations. We outlined how LTAU-FF, which avoids many of the drawbacks of previous UQ methods for atomistic force fields, can be readily applied to any model while introducing only negligible computational overhead and requiring only minor modifications to training software. Furthermore, we show that the UQ metric produced by LTAU-FF can be calibrated using a simple scaling factor, and can be used as a reliable tool for re-weighting training sets and predicting model failure during simulations. Future work applying LTAU to other deep learning tasks, or coupling LTAU-FF with more advanced clustering methods and extending it with error propagation techniques would be particularly welcome contributions. Additionally, work exploring modifications to LTAU that may further improve the diversity of the ensemble (e.g., alternative loss functions or training regimen), or analysis quantifying the effects of ensemble diversity would also be useful. Moving forward, we hope that this work will serve as a valuable tool for developing machine-learned atomistic force fields by aiding in the design of active learning workflows, failure analysis methods, and data pruning techniques.

## 6 Data and code availability

All training sets can be found at their original sources. The LTAU-FF code and all models developed in this work will be provided at <https://github.com/LLNL/ltau-ff> upon completion of internal review of the software.

## 7 Author contributions

**Joshua A. Vita:** Conceptualization, Methodology, Software, Validation, Formal analysis, Investigation, Data Curation, Writing - Original Draft, Writing - Review & Editing, Visualization. **Amit Samanta:** Methodology, Writing - Review & Editing, Supervision **Fei Zhou:** Methodology, Writing - Review & Editing, Supervision **Vincenzo Lordi:** Methodology, Resources, Writing - Review & Editing, Supervision, Project administration, Funding acquisition.

## 8 Acknowledgments

This work was performed under the auspices of the U.S. Department of Energy by Lawrence Livermore National Laboratory under Contract DE-AC52-07NA27344, funded by the Laboratory Directed Research and Development Program at LLNL under project tracking code 23-SI-006.

## References

- [ADH20] Chirag Agarwal, Daniel D’souza, and Sara Hooker. Estimating example difficulty using variance of gradients, 2020.
- [APH<sup>+</sup>21] Moloud Abdar, Farhad Pourpanah, Sadiq Hussain, Dana Rezazadegan, Li Liu, Mohammad Ghavamzadeh, Paul Fieguth, Xiaochun Cao, Abbas Khosravi, U. Rajendra Acharya, Vladimir Makarenkov, and Saeid Nahavandi. A review of uncertainty quantification in deep learning: Techniques, applications and challenges. *Information Fusion*, 76:243–297, December 2021.
- [APK12] Panagiotis Angelikopoulos, Costas Papadimitriou, and Petros Koumoutsakos. Bayesian uncertainty quantification and propagation in molecular dynamics simulations: A high performance computing framework. *The Journal of Chemical Physics*, 137(14), October 2012.
- [Bas92] M. I. Baskes. Modified embedded-atom potentials for cubic materials and impurities. *Physical Review B*, 46(5):2727–2742, August 1992.
- [BBJB<sup>+</sup>21] Jonas Busk, Peter Bjørn Jørgensen, Arghya Bhowmik, Mikkel N Schmidt, Ole Winther, and Tejs Vegge. Calibrated uncertainty for molecular property prediction using ensembles of message passing neural networks. *Machine Learning: Science and Technology*, 3(1):015012, December 2021.
- [BBK<sup>+</sup>22] Ilyes Batatia, Simon Batzner, Dávid Péter Kovács, Albert Musaelian, Gregor N. C. Simm, Ralf Drautz, Christoph Ortner, Boris Kozinsky, and Gábor Csányi. The design space of e(3)-equivariant atom-centered interatomic potentials, 2022.



- [BKS<sup>+</sup>22] Ilyes Batatia, Dávid Péter Kovács, Gregor N. C. Simm, Christoph Ortner, and Gábor Csányi. Mace: Higher order equivariant message passing neural networks for fast and accurate force fields, 2022.
- [BMS<sup>+</sup>22] Simon Batzner, Albert Musaelian, Lixin Sun, Mario Geiger, Jonathan P. Mailoa, Mordechai Kornbluth, Nicola Molinari, Tess E. Smidt, and Boris Kozinsky. E(3)-equivariant graph neural networks for data-efficient and accurate interatomic potentials. *Nature Communications*, 13(1), May 2022.
- [BP07] Jörg Behler and Michele Parrinello. Generalized neural-network representation of high-dimensional potential-energy surfaces. *Physical Review Letters*, 98(14), April 2007.
- [BPKC10] Albert P. Bartók, Mike C. Payne, Risi Kondor, and Gábor Csányi. Gaussian approximation potentials: The accuracy of quantum mechanics, without the electrons. *Physical Review Letters*, 104(13), April 2010.
- [CBFAvL20] Anders S. Christensen, Lars A. Bratholm, Felix A. Faber, and O. Anatole von Lilienfeld. Fchl revisited: Faster and more accurate quantum machine learning. *The Journal of Chemical Physics*, 152(4), January 2020.
- [CCS<sup>+</sup>16] Pratik Chaudhari, Anna Choromanska, Stefano Soatto, Yann LeCun, Carlo Baldassi, Christian Borgs, Jennifer Chayes, Levent Sagun, and Riccardo Zecchina. Entropy-SGD: Biasing Gradient Descent Into Wide Valleys. *arXiv:1611.01838*, 2016.
- [CDG<sup>+</sup>21a] Lowik Chanussot, Abhishek Das, Siddharth Goyal, Thibaut Lavril, Muhammed Shuaibi, Morgane Riviere, Kevin Tran, Javier Heras-Domingo, Caleb Ho, Weihua Hu, Aini Palizhati, Anuroop Sriram, Brandon Wood, Junwoong Yoon, Devi Parikh, C. Lawrence Zitnick, and Zachary Ulissi. Correction to “the open catalyst 2020 (oc20) dataset and community challenges”. *ACS Catalysis*, 11(21):13062–13065, October 2021.
- [CDG<sup>+</sup>21b] Lowik Chanussot, Abhishek Das, Siddharth Goyal, Thibaut Lavril, Muhammed Shuaibi, Morgane Riviere, Kevin Tran, Javier Heras-Domingo, Caleb Ho, Weihua Hu, Aini Palizhati, Anuroop Sriram, Brandon Wood, Junwoong Yoon, Devi Parikh, C. Lawrence Zitnick, and Zachary Ulissi. Open catalyst 2020 (oc20) dataset and community challenges. *ACS Catalysis*, 11(10):6059–6072, May 2021.
- [CLL17] Hugh Chen, Scott Lundberg, and Su-In Lee. Checkpoint ensembles: Ensemble methods from a single training process, 2017.
- [CMCW<sup>+</sup>23] Jesús Carrete, Hadrián Montes-Campos, Ralf Wanzenböck, Esther Heid, and Georg K. H. Madsen. Deep ensembles vs committees for uncertainty estimation in neural-network force fields: Comparison and application to active learning. *The Journal of Chemical Physics*, 158(20), May 2023.
- [DCC19] Volker L. Deringer, Miguel A. Caro, and Gábor Csányi. Machine learning interatomic potentials as emerging tools for materials science. *Advanced Materials*, 31(46), September 2019.
- [EMR<sup>+</sup>22] Romain Egele, Romit Maulik, Krishnan Raghavan, Bethany Lusch, Isabelle Guyon, and Prasanna Balaprakash. Autodeuq: Automated deep ensemble with uncertainty quantification. In *2022 26th International Conference on Pattern Recognition (ICPR)*. IEEE, August 2022.
- [Fe19] Vitaly Feldman. Does learning require memorization? a short tale about a long tail, 2019.
- [FHL19] Stanislav Fort, Huiyi Hu, and Balaji Lakshminarayanan. Deep ensembles: A loss landscape perspective, 2019.
- [FZ20] Vitaly Feldman and Chiyuan Zhang. What neural networks memorize and why: Discovering the long tail via influence estimation, 2020.
- [GBM17] Michael Gastegger, Jörg Behler, and Philipp Marquetand. Machine learning molecular dynamics for the simulation of infrared spectra. *Chemical Science*, 8(10):6924–6935, 2017.
- [GGG<sup>+</sup>21] Justin Gilmer, Behrooz Ghorbani, Ankush Garg, Sneha Kudugunta, Behnam Neyshabur, David Car-doze, George Dahl, Zachary Nado, and Orhan Firat. A loss curvature perspective on training instability in deep learning, 2021.
- [GWP<sup>+</sup>23] Kelvin Guu, Albert Webson, Ellie Pavlick, Lucas Dixon, Ian Tenney, and Tolga Bolukbasi. Simfluence: Modeling the influence of individual training examples by simulating training runs, 2023.
- [HBY<sup>+</sup>19] Alberto Hernandez, Adarsh Balasubramanian, Fenglin Yuan, Simon A. M. Mason, and Tim Mueller. Fast, accurate, and transferable many-body interatomic potentials by symbolic regression. *npj Computational Materials*, 5(1), November 2019.
- [HMUM22] Yuge Hu, Joseph Musielewicz, Zachary W Ulissi, and Andrew J Medford. Robust and scalable uncertainty estimation with conformal prediction for machine-learned interatomic potentials. *Machine Learning: Science and Technology*, 3(4):045028, December 2022.

- [HS94] Sepp Hochreiter and Jürgen Schmidhuber. Simplifying neural nets by discovering flat minima. *Advances in Neural Information Processing Systems*, 7, 1994.
- [HSY<sup>+</sup>20] Lior Hirschfeld, Kyle Swanson, Kevin Yang, Regina Barzilay, and Connor W. Coley. Uncertainty quantification using neural networks for molecular property prediction. *Journal of Chemical Information and Modeling*, 60(8):3770–3780, July 2020.
- [JDJ19] Jeff Johnson, Matthijs Douze, and Hervé Jégou. Billion-scale similarity search with GPUs. *IEEE Transactions on Big Data*, 7(3):535–547, 2019.
- [JDY<sup>+</sup>19] Jon Paul Janet, Chenru Duan, Tzuhsiung Yang, Aditya Nandy, and Heather J. Kulik. A quantitative uncertainty metric controls error in neural network-driven chemical discovery. *Chemical Science*, 10(34):7913–7922, 2019.
- [Jon24] J. E. Jones. On the determination of molecular fields. —II. from the equation of state of a gas. *Proceedings of the Royal Society of London. Series A, Containing Papers of a Mathematical and Physical Character*, 106(738):463–477, October 1924.
- [KOK<sup>+</sup>21] Dávid Péter Kovács, Cas van der Oord, Jiri Kucera, Alice E. A. Allen, Daniel J. Cole, Christoph Ortner, and Gábor Csányi. Linear atomic cluster expansion force fields for organic molecules: Beyond rmse. *Journal of Chemical Theory and Computation*, 17(12):7696–7711, November 2021.
- [KSR<sup>+</sup>21] Krishnateja Killamsetty, Durga Sivasubramanian, Ganesh Ramakrishnan, Abir De, and Rishabh Iyer. Grad-match: Gradient matching based data subset selection for efficient deep model training, 2021.
- [KSRI20] Krishnateja Killamsetty, Durga Sivasubramanian, Ganesh Ramakrishnan, and Rishabh Iyer. Glister: Generalization based data subset selection for efficient and robust learning. 2020.
- [KZ22] Leonid Kahle and Federico Zipoli. Quality of uncertainty estimates from neural network potential ensembles. *Physical Review E*, 105(1), January 2022.
- [LGC<sup>+</sup>23] Shuaihua Lu, Luca M. Ghiringhelli, Christian Carbogno, Jinlan Wang, and Matthias Scheffler. On the uncertainty estimates of equivariant-neural-network-ensembles interatomic potentials, 2023.
- [LPB16] Balaji Lakshminarayanan, Alexander Pritzel, and Charles Blundell. Simple and scalable predictive uncertainty estimation using deep ensembles, 2016.
- [LW18] Ruifeng Liu and Anders Wallqvist. Molecular similarity-based domain applicability metric efficiently identifies out-of-domain compounds. *Journal of Chemical Information and Modeling*, 59(1):181–189, November 2018.
- [LXT<sup>+</sup>17] Hao Li, Zheng Xu, Gavin Taylor, Christoph Studer, and Tom Goldstein. Visualizing the loss landscape of neural nets, 2017.
- [MBJ<sup>+</sup>23] Albert Musaelian, Simon Batzner, Anders Johansson, Lixin Sun, Cameron J. Owen, Mordechai Kornbluth, and Boris Kozinsky. Learning local equivariant representations for large-scale atomistic dynamics. *Nature Communications*, 14(1), February 2023.
- [MBL19] Baharan Mirzasoleiman, Jeff Bilmes, and Jure Leskovec. Coresets for data-efficient training of machine learning models. 2019.
- [MC20] Sergei Manzhos and Tucker Carrington. Neural network potential energy surfaces for small molecules and reactions. *Chemical Reviews*, 121(16):10187–10217, October 2020.
- [MHW20] Tim Mueller, Alberto Hernandez, and Chuhong Wang. Machine learning for interatomic potential models. *The Journal of Chemical Physics*, 152(5), February 2020.
- [Mis21] Y. Mishin. Machine-learning interatomic potentials for materials science. *Acta Materialia*, 214:116980, August 2021.
- [MY16] Yu. A. Malkov and D. A. Yashunin. Efficient and robust approximate nearest neighbor search using hierarchical navigable small world graphs, 2016.
- [PCK17] Andrew A. Peterson, Rune Christensen, and Alireza Khorshidi. Addressing uncertainty in atomistic machine learning. *Physical Chemistry Chemical Physics*, 19(18):10978–10985, 2017.
- [Per22] Pascal Pernot. The long road to calibrated prediction uncertainty in computational chemistry. *The Journal of Chemical Physics*, 156(11), March 2022.
- [PGD21] Mansheej Paul, Surya Ganguli, and Gintare Karolina Dziugaite. Deep learning on a data diet: Finding important examples early in training. 2021.
- [PLSK20] Garima Pruthi, Frederick Liu, Mukund Sundararajan, and Satyen Kale. Estimating training data influence by tracing gradient descent, 2020.

- [PZEW20] Geoff Pleiss, Tianyi Zhang, Ethan R. Elenberg, and Kilian Q. Weinberger. Identifying mislabeled data using the area under the margin ranking, 2020.
- [RDG<sup>+</sup>20] Patrick Rowe, Volker L. Deringer, Piero Gasparotto, Gábor Csányi, and Angelos Michaelides. An accurate and transferable machine learning potential for carbon. *The Journal of Chemical Physics*, 153(3), July 2020.
- [RNE<sup>+</sup>22] Patrick Reiser, Marlen Neubert, André Eberhard, Luca Torresi, Chen Zhou, Chen Shao, Houssam Metni, Clint van Hoesel, Henrik Schopmans, Timo Sommer, and Pascal Friederich. Graph neural networks for materials science and chemistry. *Communications Materials*, 3(1), November 2022.
- [RTH<sup>+</sup>22] Stephan Rabanser, Anvith Thudi, Kimia Hamidieh, Adam Dziedzic, and Nicolas Papernot. Selective classification via neural network training dynamics, 2022.
- [SCQvdS23] Nabeel Seedat, Jonathan Crabbé, Zhaozhi Qian, and Mihaela van der Schaar. Triage: Characterizing and auditing training data for improved regression, 2023.
- [SGS<sup>+</sup>22] Ben Sorscher, Robert Geirhos, Shashank Shekhar, Surya Ganguli, and Ari S. Morcos. Beyond neural scaling laws: beating power law scaling via data pruning, 2022.
- [SSL<sup>+</sup>20] Swabha Swayamdipta, Roy Schwartz, Nicholas Lourie, Yizhong Wang, Hannaneh Hajishirzi, Noah A. Smith, and Yejin Choi. Dataset cartography: Mapping and diagnosing datasets with training dynamics, 2020.
- [SUG21] Kristof T. Schütt, Oliver T. Unke, and Michael Gastegger. Equivariant message passing for the prediction of tensorial properties and molecular spectra, 2021.
- [TNY<sup>+</sup>20] Kevin Tran, Willie Neiswanger, Junwoong Yoon, Qingyang Zhang, Eric Xing, and Zachary W Ulissi. Methods for comparing uncertainty quantifications for material property predictions. *Machine Learning: Science and Technology*, 1(2):025006, May 2020.
- [TSC<sup>+</sup>18] Mariya Toneva, Alessandro Sordoni, Remi Tachet des Combes, Adam Trischler, Yoshua Bengio, and Geoffrey J. Gordon. An empirical study of example forgetting during deep neural network learning, 2018.
- [TUG<sup>+</sup>23] Aik Rui Tan, Shingo Urata, Samuel Goldman, Johannes C. B. Dietschreit, and Rafael Gómez-Bombarelli. Single-model uncertainty quantification in neural network potentials does not consistently outperform model ensembles. 2023.
- [vDDL01] Adri C. T. van Duin, Siddharth Dasgupta, Francois Lorant, and William A. Goddard. ReaxFF: a reactive force field for hydrocarbons. *The Journal of Physical Chemistry A*, 105(41):9396–9409, October 2001.
- [VSK23] Joshua A Vita and Daniel Schwalbe-Koda. Data efficiency and extrapolation trends in neural network interatomic potentials. *Machine Learning: Science and Technology*, 4(3):035031, August 2023.
- [WGC<sup>+</sup>23] Tom Wollschläger, Nicholas Gao, Bertrand Charpentier, Mohamed Amine Ketata, and Stephan Günemann. Uncertainty estimation for molecules: Desiderata and methods, 2023.
- [WSC21] Shunzhou Wan, Robert C. Sinclair, and Peter V. Coveney. Uncertainty quantification in classical molecular dynamics. *Philosophical Transactions of the Royal Society A: Mathematical, Physical and Engineering Sciences*, 379(2197), March 2021.
- [WT20] Mingjian Wen and Ellad B. Tadmor. Uncertainty quantification in molecular simulations with dropout neural network potentials. *npj Computational Materials*, 6(1), August 2020.
- [WWS<sup>+</sup>23] Zun Wang, Hongfei Wu, Lixin Sun, Xinheng He, Zhirong Liu, Bin Shao, Tong Wang, and Tie-Yan Liu. Improving machine learning force fields for molecular dynamics simulations with fine-grained force metrics. *The Journal of Chemical Physics*, 159(3), July 2023.
- [XVS<sup>+</sup>21] Yu Xie, Jonathan Vandermause, Lixin Sun, Andrea Cepellotti, and Boris Kozinsky. Bayesian force fields from active learning for simulation of inter-dimensional transformation of stanene. *npj Computational Materials*, 7(1), March 2021.
- [ZBMK23] Albert Zhu, Simon Batzner, Albert Musaelian, and Boris Kozinsky. Fast uncertainty estimates in deep learning interatomic potentials. *The Journal of Chemical Physics*, 158(16), April 2023.
- [ZLP<sup>+</sup>22] Xinlei Zhou, Han Liu, Farhad Pourpanah, Tieyong Zeng, and Xizhao Wang. A survey on epistemic (model) uncertainty in supervised learning: Recent advances and applications. *Neurocomputing*, 489:449–465, June 2022.

## A Hyperparameter details

### A.1 NequIP

Table A1 outlines some of the most important parameters used for defining the NequIP architecture, the training algorithm, or computing the  $\mu_M(p_i)$  values for each dataset. Unless otherwise specified, the recommended settings were used for the NequIP model as provided by <https://github.com/mir-group/nequip/blob/main/configs/full.yaml>. For 3BPA the predefined training set was used with no validation set. For Carbon\_GAP\_20 a random 90-10 training-validation split was used. For OC20 the predefined S2EF training set and IS2RS validation sets were used. The AMSGrad variant of the Adam optimizer was used, with an initial learning rate of 0.005, a weight decay of 0, and the ReduceLROnPlateau scheduler. Full configuration files will be provided upon completion of internal review of the software.

Table A1: The main hyperparameters used for the NequIP model. `r_max` is the radial cutoff of the model, `num_layers` is the number of message passing layers, `l_max` is the symmetry order of the equivariant features, and  $M$  is the ensemble size.

Dataset	r_max	num_layers	l_max	F loss weight	E loss weight	Batch size	$M$
3BPA	5.0	5	3	1000.0	0.0	5	10
Carbon_GAP_20	4.5	4	2	10.0	0.0	1	20
OC20	4.0	2	2	100.0	1.0	4	1

### A.2 FAISS

The cost of UQ predictions with LTAU-FF is dictated by the complexity of the similarity search performed by the FAISS package, as well as the size of the training set and the dimensionality of the latent space embeddings used as the atomic descriptors. Depending on these factors, particularly the dataset size, different indexing algorithms (as implemented by FAISS) are recommended. For the Carbon\_GAP\_20 and OC20 datasets, the approximate neighbor search IndexHNSWFlat index was used as opposed to the exact brute-force approach (IndexFlatL2) used for 3BPA. Additional UQ speedups could be obtained by using the GPU implementation of FAISS, decreasing  $k$ , or further refining the parameters of the indexers. For a more thorough discussion of indexing methods and hyperparameter choices, we recommend consulting the FAISS documentation.

While the IndexFlatL2 index is a parameter-free brute force approach, the IndexHNSWFlat index has two primary parameters which strongly affect the cost of the similarity search. The Heirarchical Navigable Small Worlds (HNSW) method [MY16] is an *approximate* similarity search algorithm which decomposes the search space into a multi-layered graph structure. The key parameters of IndexHNSWFlat are  $M$  (the number of neighbor links to add for each point in the graph), `efConstruction` (the number of neighbors to consider at each layer when inserting into the graph), and `efSearch` (the number of neighbors to consider at each layer when searching the graph). In this work, we used values of  $M=32$ , `efConstruction`= 40, and `efSearch`= 16, which we found to provide a reasonable balance between speed and accuracy. The computational cost of model evaluation using these hyperparameters are shown in Table A2, where the number of nearest-neighbors searched for is specified as  $k$ . We emphasize that more thorough analysis of the effects of tuning these hyperparameters would be helpful.

Table A2: Computational costs of evaluating model uncertainty for the datasets used in this work. Results were obtained by computing forces and uncertainties for a single NequIP model on a random selection of 5000 test samples for each dataset (500 for 3BPA).

Dataset	Train size (# atoms)	Operation	% time
3BPA	13,500	UQ (IndexFlatL2, $k=2$ )	0.9
		Graph construction	32.9
		Forward pass	65.9
Carbon_GAP_20	400,275	UQ (IndexHNSWFlat, $k=10$ )	1.0
		Graph construction	53.8
		Forward pass	44.9
OC20	14,631,937	UQ (IndexHNSWFlat, $k=10$ )	5.0
		Graph construction	21.3
		Forward pass	73.1

Table B1: Number of atomic configurations and atoms within each group of the Carbon\_GAP\_20 training set.

config_type group	# configurations	# atoms
Amorphous_Bulk	3,053	200,470
Amorphous_Surfaces	20	2,648
Crystalline_Bulk	78	368
Crystalline_RSS	483	8,554
Defects	530	70,022
Diamond	164	1,360
Dimer	26	52
Fullerenes	272	11,782
Graphene	2	400
Graphite	185	6,344
Graphite_Layer_Sep	7	700
LD_iter1	80	14,048
Liquid	6	1,296
Liquid_Interface	17	3,672
Nanotubes	138	4,976
SACADA	755	24,503
Surfaces	271	49,079
Total	6,088	400,275

## B Dataset details

### 3BPA

The first dataset used in this work is the 3BPA dataset [KOK<sup>+</sup>21], which has been used previously in the literature for benchmarking extrapolation behaviors of force fields [BKS<sup>+</sup>22, BBK<sup>+</sup>22, MBJ<sup>+</sup>23]. The 3BPA dataset is a molecular dataset consisting of 500 training configurations taken from molecular dynamics (MD) simulations at a temperature of 300 K, where each configuration has 27 atoms for a total of 13,500 training points. There are additionally three separate test sets sampled using MD simulations at temperatures of 300K, 600K, and 1200K, respectively, where increasing the sampling temperature can be expected to push the simulations to explore OOD regions of the available configuration space of the molecule.

### Carbon\_GAP\_20

In order to better understand how LTAU-FF performs on a more challenging dataset, we also used the Carbon\_GAP\_20 dataset [RDG<sup>+</sup>20], which was originally intended to be used for fitting a model capable of accurately describing a broad range of carbon phases. The Carbon\_GAP\_20 dataset includes a training set of 6,088 configurations (400,275 atoms), as well as a larger superset containing 17,525 configurations (1,345,246 atoms) which we used for testing. The training and test sets are comprised of an extremely diverse range of phases, including bulk crystals, amorphous carbon, graphene, graphite, fullerene, nanotubes, liquids, surfaces, defected configurations, and other rare allotropes obtained through random structure search or extracted from the literature. Particularly valuable for our purposes are the labels provided by the authors of the Carbon\_GAP\_20 dataset for defining conceptually similar clusters over the atomic configurations in the dataset. Although in our analysis we observed a number of mislabeled configurations, the provided groupings are still extremely useful for understanding how the models and methods used in this work perform across different subsets of the data. A breakdown of the number of atoms in each group in the training set is provided in Table B1. A more thorough description of the dataset can be found in [RDG<sup>+</sup>20].

### OC20

As a practical application, we also train a model to the S2EF task of the OC20 dataset [CDG<sup>+</sup>21b] then test how well the UQ estimate provided by LTAU-FF predicted performance on the ISR2S task. Specifically, we trained to the 200k split (14,631,937 atoms) of the S2EF task, and tested on the val\_id and val\_ood\_both splits of the ISR2S task. The OC20 dataset includes a wide range of catalysts comprised of various materials, surfaces, and adsorbates. Importantly, the data includes labels for each atom identifying them as an “adsorbate” atom (part of the adsorbing molecule), a “surface” atom (the top few layers of the material), or a “bulk” atom (everything in the material that is not part of the surface).



## C Additional analysis of sample confidences

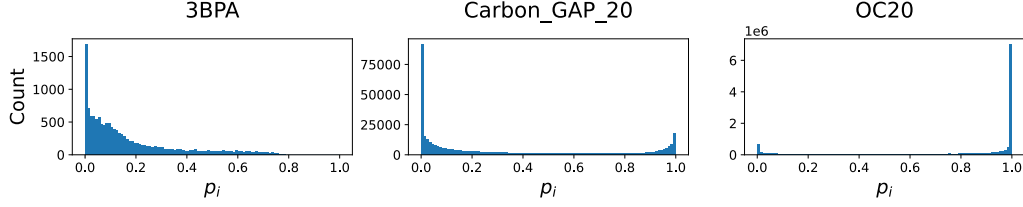


Figure C1: Distributions of the  $p_i$  values computed for all three datasets. Note that the uncertainty predicted by LTAU is  $1 - p_i$ , so a “sharper” metric is one which predicts  $p_i$  values closer to 1. A more “disperse” metrics is one with a wider range of  $p_i$  values.

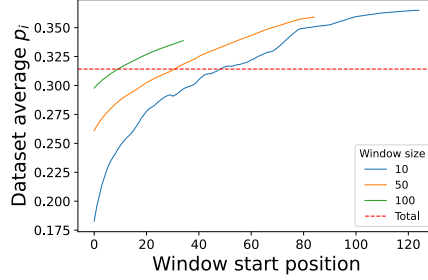


Figure C2: Effects of window size and starting position on the average  $\mu_M(p_i)$  value computed over the entire Carbon\_GAP\_20 dataset.  $\mu_M(p_i)$  values are computed over sliding windows of different sizes for every possible starting position given the trajectory of 134 epochs. The *atol* threshold is held constant at 0.265 eV/Å (the final training MAE).

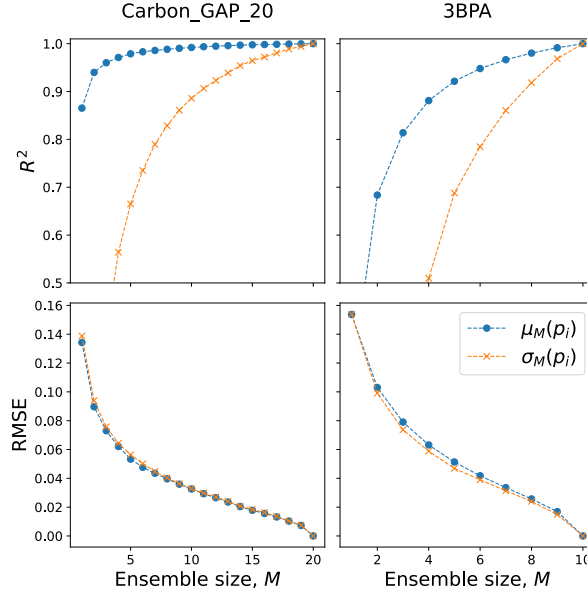


Figure C3: Convergence tests for  $\mu_M(p_i)$  and  $\sigma_M(p_i)$  with increasing  $M$ .

## D When should a scaling factor work?

The results shown in Fig. 1 and Fig. 2, while valuable for their demonstration of a practical approach to calibrating our UQ metric, raise some interesting questions about the distribution of errors and uncertainties within the latent space of

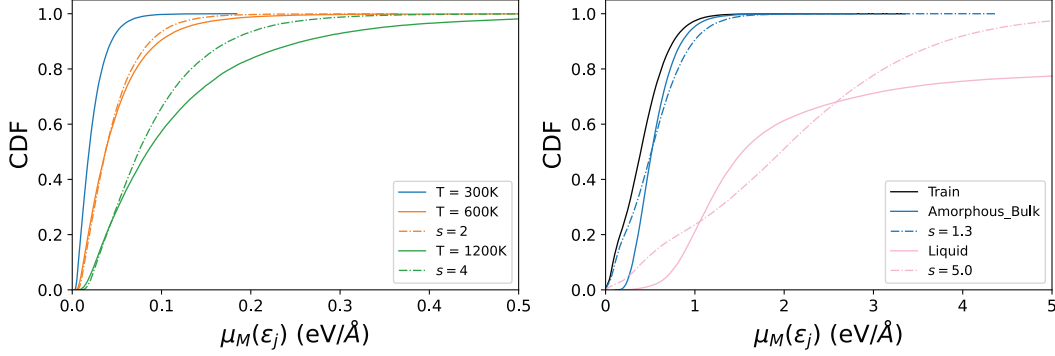


Figure D1: Qualitative analysis of the effects of scaling on the CDFs. The observed CDFs computed over an ensemble of  $M$  models are plotted as solid lines, while scaled versions of the reference CDF are plotted as dashed lines. In panel **a**, the high-temperature test CDFs from the 3BPA dataset are compared to the low-temperature test CDF, where the scaling factors,  $s$ , are specified in the legend and match those used in Fig. 1. In panel **b**, select subsets were chosen from Carbon\_GAP\_20 to exemplify a group for which a reasonable  $s$  value could be found (Amorphous\_Bulk) as well as one which could not be easily calibrated to (Liquid).

the model. The most obvious of these is: why is a simple scaling factor,  $s$ , sufficient for calibrating the UQ metric to test points? We believe that a partial answer to this question can be obtained by understanding two key aspects of the error distributions, which will be discussed further here. However, we also emphasize that future work analyzing this question further is necessary and would be quite valuable to the field.

The first aspect that should be considered is how the CDFs of the test sets relate to those of the training sets. To begin with, we will only consider the CDFs of the 3BPA dataset shown in Fig. D1a due to their relative simplicity. Recall that the  $\mu_M(p_i)$  values computed for the training points correspond to the CDF of the errors on those points evaluated at *atol*, which was taken to be the MAE of the training set. The scaling factors,  $s$ , can then be thought of as scaling the CDF of the training set in an attempt to match it to the observed CDF of the test set. Critically, if the test CDF is a scaled version of the train CDF, then the  $\mu_M(p_i)$  values from the training set may be expected to reasonably approximate the  $p_j$  values for the test set at the scaled threshold value of  $atol \times s$ . The qualitative analysis of these CDFs shown in Fig. D1a coupled with the results shown in Fig. 1c support this hypothesis, given that the scaled 300K CDF seems to be a reasonable approximation of the 600K/1200K CDFs. However, we note that the mismatch between the CDFs is significantly larger at 1200K, which is consistent with intuition that the scaling approach should begin to fail when moving further OOD. For the Carbon\_GAP\_20 dataset, where accurate calibration proved more difficult for some of the groups, we observe in Fig. D1b that the CDF of a problematic test group (Liquid) is not well represented by the scaled training CDF. This discrepancy suggests that a more advanced calibration technique may be necessary for problematic subsets of the data.

Good agreement between the test CDF and the scaled training CDF, however, is not sufficient for ensuring that testing  $p_j$  values will be similar to the  $\mu_M(p_i)$  values from their nearest training points. For example, one can imagine a scenario where the train/test sets are identical, but their point-wise errors (and corresponding uncertainties) are shuffled versions of each other. In this situation, the two sets would have identical CDFs, but the nearest neighbor training  $\mu_M(p_i)$  values would be completely uncorrelated from the observed test  $p_j$  values. In order for our UQ metric computed on the training set to be applicable to points from the test set (after scaling), it is also necessary that: 1) the test set be close enough to the training set that a distance-based similarity search yields related training points, and 2) the UQ metric be relatively uniform over the  $k$  nearest neighbors returned by the similarity search. We observe in Fig. D2 that the 3BPA dataset appears to have both of these properties, where Fig. D2a shows that the test sets are not too far OOD, and Fig. D2b shows the relative uniformity of  $\mu_M(p_i)$  within each cluster.

In the UMAP plots of the Carbon\_GAP\_20 dataset (Fig. D3 and Fig. D4), we found that there was a lack of obvious clustering in the latent space, and that the  $\mu_M(p_i)$  values were generally much noisier. Together, these two attributes make it difficult to draw conclusions about why the scaling approach does, or does not, work for specific groups. However, given the results in Fig. 2 and Fig. D1b, it seems likely that there are non-obvious regions of the latent manifold for which the scaling approach is valid. While using a larger ensemble size,  $M$ , and number of neighbors,  $k$ , when performing the similarity search can help to reduce noise in the  $\mu_M(p_i)$  values, we believe that future work developing more advanced clustering techniques could also be helpful for identifying appropriate subsets when attempting to calibrate the UQ metric via scaling.

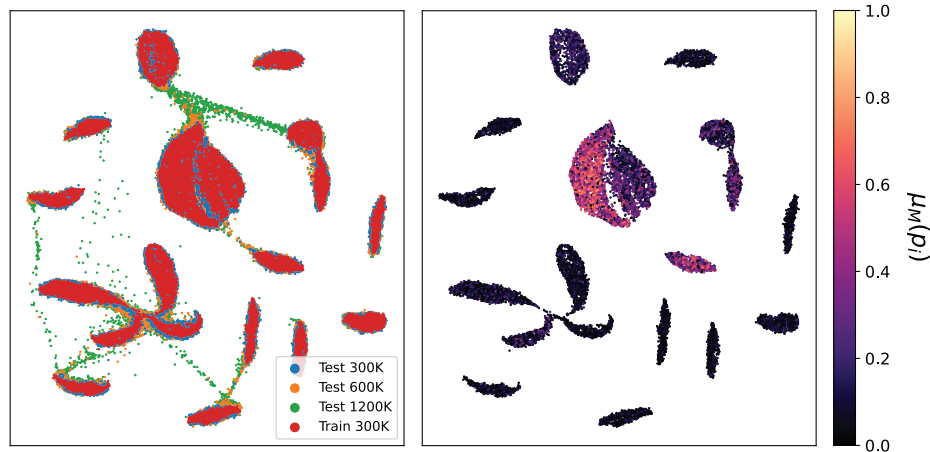


Figure D2: UMAP plots of the 3BPA dataset. Panel **a** shows the train set and all three test sets, while panel **b** shows only the train set with the points colored by their  $\mu_M(p_i)$  values. The uniformity of  $\mu_M(p_i)$  within each cluster, as well as the relative similarity between the train/test data are necessary conditions for applicability of distance-based UQ metrics, including the one developed in this work.

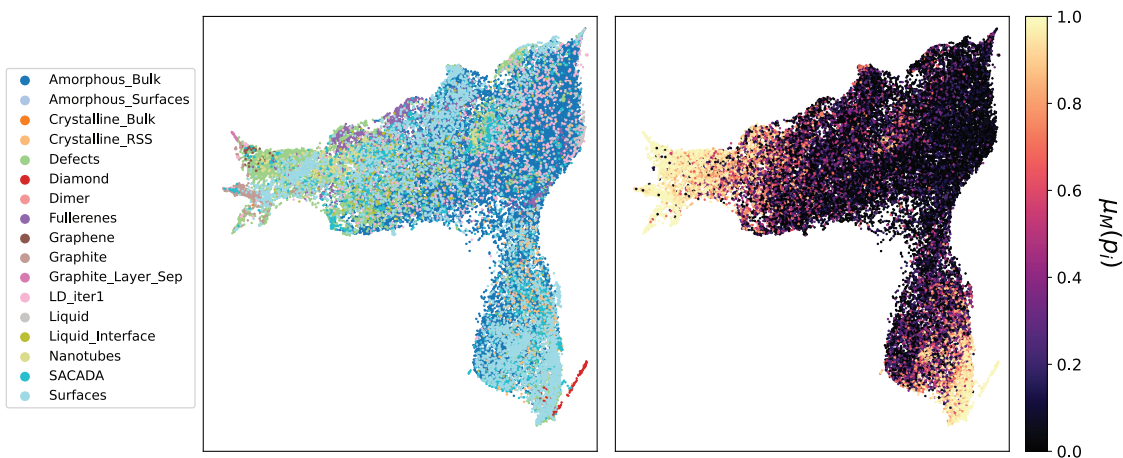


Figure D3: UMAP plots of a random sub-sample of the Carbon\_GAP\_20 dataset. Only 10% of the dataset was used in this plot for ease of visualization. For a visualization of the full dataset, see Fig. D4. The lack of clear clusters in panel **a**, as well as the noise in the  $\mu_M(p_i)$  values observed in panel **b** make it difficult to understand how to properly calibrate the UQ metric to individual groups in the dataset.

## E Dataset re-weighting

In the case of the “up-weight hard” weighting scheme in Fig. 3, atom  $i$  was given a weight in the loss function of  $w_i = \exp[\lambda(1 - \mu_M(p_i) + \sigma_M(p_i))]$ ; in the “up-weight easy” scheme, the weight was given as  $w_i = \exp[\lambda(\mu_M(p_i) + \sigma_M(p_i))]$ . Values of  $\lambda$  were determined *ad hoc*, and set to 2.0 and 4.5 for the up-weight easy and hard schemes, respectively. Fig. E1 provides a visual depiction of the two weighting schemes. Notably, the relationship between  $\mu_M(p_i)$  and  $\sigma_M(p_i)$  observed in Fig. E1 exactly follows the expected pattern from [SSL<sup>+</sup>20], where the dataset can be roughly divided into “easy-to-learn”, “hard-to-learn”, and “ambiguous” subsets.

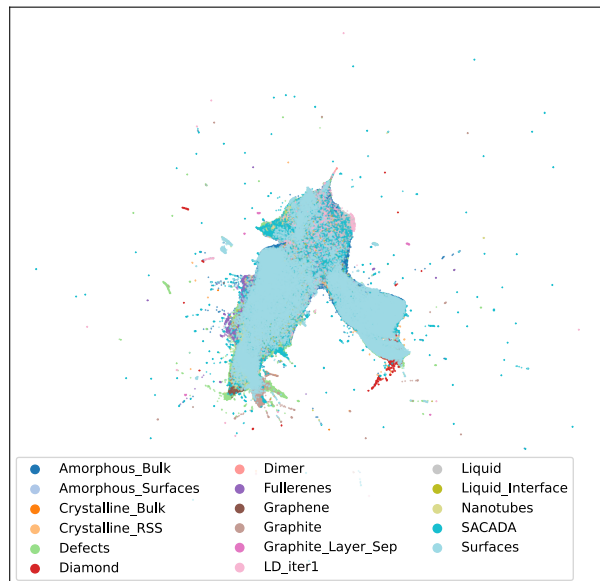


Figure D4: UMAP plot of the full Carbon\_GAP\_20 dataset. The outlying clusters highlight the need for further analysis and improved clustering techniques to refine the calibration of the UQ metric for more complex datasets.

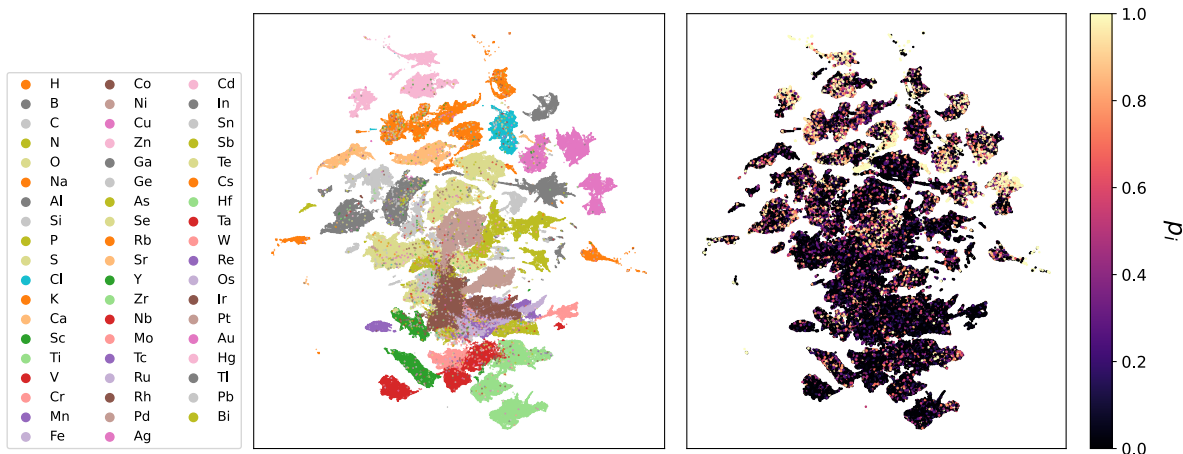


Figure D5: UMAP plots of a random sub-sample of the OC\_20 dataset. Only 2% of the dataset was used in this plot for ease of visualization. Points are colored according to their group on the periodic table (panel **a**) or their  $p_i$  value (panel **b**). Note the use of  $p_i$  instead of  $\mu_M(p_i)$  because even the 200k split of the S2EF task was too expensive to train more than a single model without multi-GPU support from the NequIP code. Interestingly, though perhaps unsurprisingly, the model appears to learn to cluster atoms by their group on the periodic table.

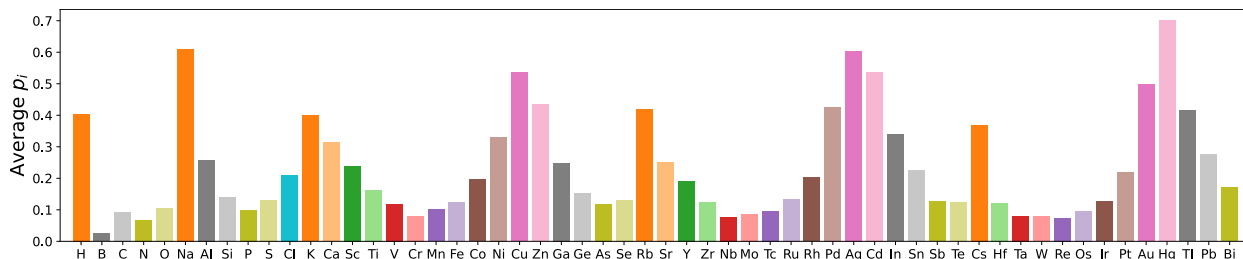


Figure D6: Averaged  $p_i$  values for each element type, colored by group on the periodic table. The  $p_i$  values seem to follow a similar trend to that observed in Fig. D5, likely due to the relative magnitudes of the target forces for each element type.

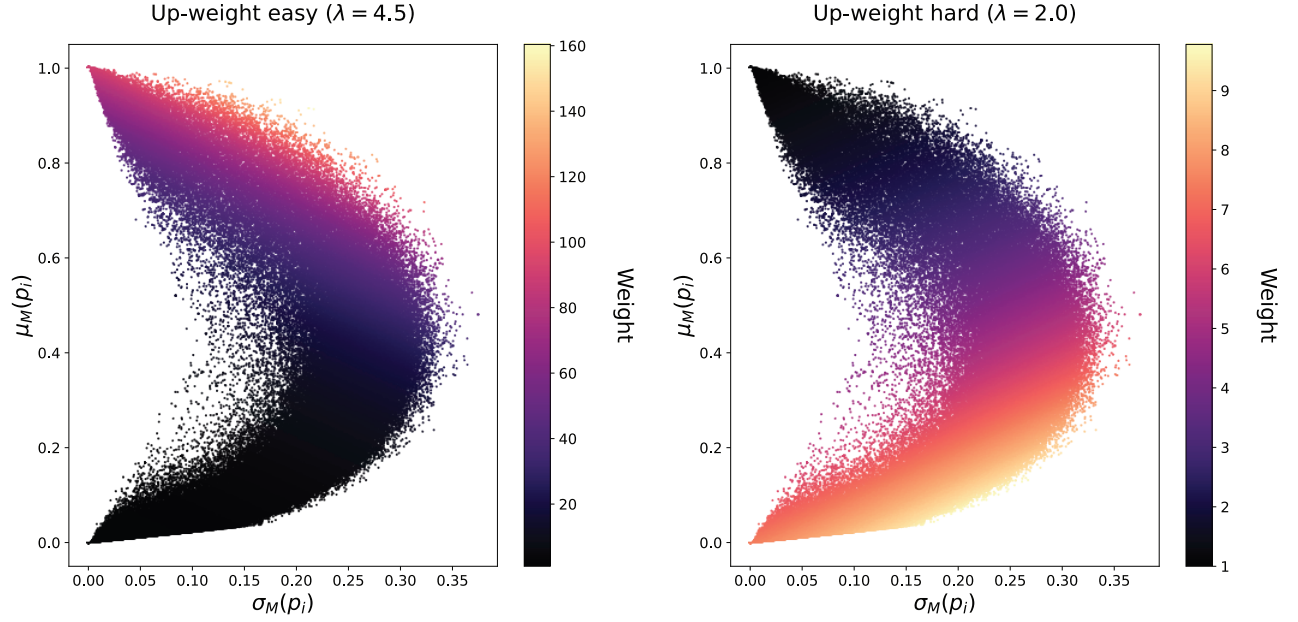


Figure E1: Visualization of the re-weighting schemes used for the Carbon\_GAP\_20 dataset in Fig. 3. Scaling factors,  $\lambda$ , were selected *ad hoc* based on experimentation in order to obtain weights which resulted in a noticeable change in the training–validation gap as shown in Fig. 3.

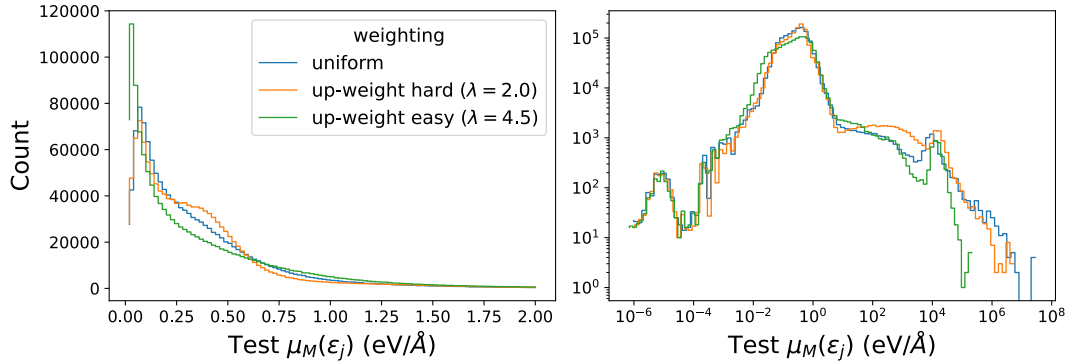


Figure E2: Distributions of test errors on the Carbon\_GAP\_20 dataset for the three weighting schemes. In panel **a**, the range of the x-axis has been clipped to a maximum value of 2.0 eV/Å in order to improve visualization by removing a small number (3–4%) of points with abnormally large errors. In panel **b**, the full distributions are shown on a log-scale. The average test error for all weighting schemes after removing values larger than 2.0 eV/Å, was around 0.35 eV/Å. However, when including all data from panel **b**, the “up-weight easy” scheme had an MAE of 47 eV/Å, which was an order of magnitude lower than the other two schemes.